Insights into anisotropy development and weakening of ice from in situ *P* wave velocity monitoring during laboratory creep

M. J. Vaughan[1] iD **, D. J. Prior[1]** iD **, M. Jefferd[2]** iD **, N. Brantut[2]** iD **, T. M. Mitchell[2]** iD **, and M. Seidemann[1]**

[1]Department of Earth Sciences, University of Otago, Dunedin, New Zealand, [2]Rock and Ice Physics Laboratory, Department of Earth Sciences, University College London, London, UK

Abstract Polycrystalline ice weakens significantly after a few percent strain, during high homologous temperature deformation. Weakening is correlated broadly with the development of a crystallographic preferred orientation (CPO). We deformed synthetic polycrystalline ice at −5°C under uniaxial compression, while measuring ultrasonic *P* wave velocities along several raypaths through the sample. Changes in measured *P* wave velocities (V_p) and in the velocities calculated from microstructural measurements of CPO (by cryo-electron backscatter diffraction) both show that velocities along trajectories parallel and perpendicular to shortening decrease with increasing strain, while velocities on diagonal trajectories increase. Thus, in these experiments, velocity data provide a continuous measurement of CPO evolution in creeping ice. Samples reach peak stresses after 1% shortening. Weakening corresponds to the start of CPO development, as indicated by divergence of *P* wave velocity changes for different raypaths, and initiates at ≈3% shortening. Selective growth by strain-induced grain boundary migration (GBM) of grains favorably oriented for basal slip may initiate weakening through the formation of an interconnected network of these grains by 3% shortening. After weakening initiates, CPO continues to develop by GBM and nucleation processes. The resultant CPO has an open cone (small circle) configuration, with the cone axis parallel to shortening. The development of this CPO causes significant weakening under uniaxial compression, where the shear stresses resolved on the basal planes (Schmid factors) are high.

1. Introduction

At terrestrial conditions, ice 1h exhibits high viscoplastic anisotropy, with dislocation glide being easiest by more than an order of magnitude along basal planes [*Duval et al.*, 2010; *Duval and Castelnau*, 1995]. This leads to the development of strong crystallographic preferred orientations (CPOs) during deformation in the dislocation creep regime. CPOs change the creep behavior significantly [*Azuma*, 1995], generally weakening the ice for flow compared to a random CPO. However, CPOs evolve as ice accumulates strain [*Faria et al.*, 2014; *Wilson et al.*, 2014] and any change in deformation kinematics, flow stress, or temperature will likely modify the CPO and resultant micromechanics of creep.

With an ever increasing interest in the role polar ice sheets play in controlling sea level rise, understanding the flow of ice on the microstructural scale has become increasingly important [*Llorens et al.*, 2016; *Montagnat et al.*, 2014]. An improved knowledge of large-scale ice dynamics, and thus our ability to predict future changes of ice sheets, is limited by our understanding of the microstructural mechanics of ice [*Alley*, 1992; *Treverrow et al.*, 2015]. Constraining the mechanisms and rates by which CPOs and corresponding mechanical behavior evolve will be crucial to understanding how ice flow properties develop as boundary conditions change (e.g., grounding zones where ice streams flow into ice shelves), in the Antarctic or Greenland ice sheets [*Bamber et al.*, 2000; *Rignot et al.*, 2011; *Zwinger et al.*, 2014]. It is fundamentally important to understand the response of ice sheets to climate change and their future contributions to sea level rise [*Pollard and DeConto*, 2009].

In laboratory experiments, ice weakens after very small strains, corresponding to the transition from secondary to tertiary creep. At high homologous temperatures (temperature of a material as a fraction of its melting point temperature, in degrees Kelvin), weakening and associated CPO development is strongly influenced by mechanisms of dynamic recrystallization, which relax the internal stress fields induced by strong

strain heterogeneities between neighboring grains [*Duval et al.*, 1983; *Schulson et al.*, 2009]. Nucleation processes associated with recrystallization in ice [*Chauve et al.*, 2017a] must also play a role, as decreases in median grain sizes have been observed as a function of strain [*Montagnat et al.*, 2015; *Piazolo et al.*, 2013; *Peternell and Wilson*, 2016]. At high temperatures, CPOs evolve dominantly through recrystallization by rapid grain boundary migration (GBM), termed "migration recrystallization" [*Thorsteinsson et al.*, 1997; *De La Chapelle et al.*, 1998; *Montagnat et al.*, 2015] in the glaciological community. While macroscopic weakening is broadly related to the combination of CPO development and mechanisms of dynamic recrystallization [*De La Chapelle et al.*, 1998; *Faria et al.*, 2014; *Hudleston*, 2015; *Piazolo et al.*, 2013; *Wilson et al.*, 2014], a comprehensive and satisfactory understanding of this relationship does not currently exist, for ice or other rock-forming minerals.

The majority of ice deformation experiments that show microstructures and CPOs do so for the start and end of experiments only. Some studies conduct several experiments with equivalent starting materials to different finite strains [e.g., *Jacka and Maccagnan*, 1984; *Montagnat et al.*, 2015] to get a strain series. Quasi-continuous CPO and grain size measurements have been made during deformation experiments using neutron diffraction [*Piazolo et al.*, 2013; *Wilson et al.*, 2014, 2015; *Cyprych et al.*, 2016]. Quasi-continuous microstructural analysis and CPO measurements have also been made using synkinematic optical microscopy [*Peternell et al.*, 2014; *Wilson et al.*, 2014; *Peternell and Wilson*, 2016]. These experiments that track the development of CPO as a function of strain (or time) provide new insight into the relationships of CPO development to mechanical evolution. The methods used have limitations. The neutron beam approach requires D_2O ice, becomes problematic for nonsymmetric samples, and, because experiments need to be fast (beam time is limited), is limited to high strain rates. The experiments are unconfined so that high temperatures are required to allow high strain rates. The synkinematic microscopy approaches have limited sample sizes and do not provide robust mechanical data. We looked to ultrasonic wave velocities to provide quasi-continuous measurements of CPO evolution during ice experiments.

Much work has been undertaken to quantify the relationship between CPO and elastic wave velocity anisotropy using measurements in natural samples and boreholes [*Kohnen and Gow*, 1979; *Bentley*, 1972; *Anandakrishnan and Alley*, 1994; *Gusmeroli et al.*, 2012; *Kluskiewicz et al.*, 2017], modeling techniques [*Diez and Eisen*, 2015; *Maurel et al.*, 2015], and recently to infer CPO from active-source seismic field measurements [*Picotti et al.*, 2015; *Vélez et al.*, 2016] and passive listening to natural events at the base of flowing ice [*Smith et al.*, 2017; *Harland et al.*, 2013]. In situ real-time ultrasonic velocity measurements have been used to monitor physical property evolution during brittle rock deformation experiments [*Ayling et al.*, 1995; *Guillaume et al.*, 1997; *Fortin et al.*, 2007; *Stanchits et al.*, 2010; *Fortin et al.*, 2011; *Brantut et al.*, 2011, 2014]. Experiments that make such measurements during high-temperature ductile creep have only been achieved with metals [*Hirao et al.*, 1990; *Tang et al.*, 2007] and never before with rock or ice samples.

In this paper we make in situ ultrasonic velocity measurements during deformation experiments on ice at high homologous temperatures. We chose deformation conditions and kinematics where the CPOs are already well known [*Budd and Jacka*, 1989; *Wilson et al.*, 2014; *Montagnat et al.*, 2015] so that we can assess fully the new information from the ultrasonic velocity measurements. Our approach was to conduct experiments to different final strains, with repeated (every 5 min) *P* wave velocity measurements, so that final microstructures and CPO measured using cryo-electron backscatter diffraction (cryo-EBSD) [*Prior et al.*, 2015] could be compared with *P* wave velocity data at the end of each experiment. The overall objective was to assess ultrasonic velocity measurements as a proxy for CPO development during ice deformation and to explore the new information that the proxy yields.

2. Methods

In this section, we outline the details of sample manufacturing and the deformation conditions (2.1), the measurement of ultrasonic travel times (2.2), and the acquisition of cryo-EBSD data (2.3).

2.1. Samples and Deformation

We prepared cylindrical samples (40 mm diameter, 95–100 mm long) of polycrystalline ice (derived from distilled and deionized water) using the "standard" ice method [*Stern et al.*, 1997]. We began by filling a mold (supporting information Figure S1) with controlled grain size seed ice (200–250 µm), evacuating the air out of the mold and flooding it with degassed (by boiling) water at 0°C. Once flooded, we encased the samples in an insulated sleeve and placed them in a chest freezer at −30°C. We froze the samples uniaxially from the base (with the bottom of the sample mold resting on a cold copper plate) to prevent cracking, extracted them,
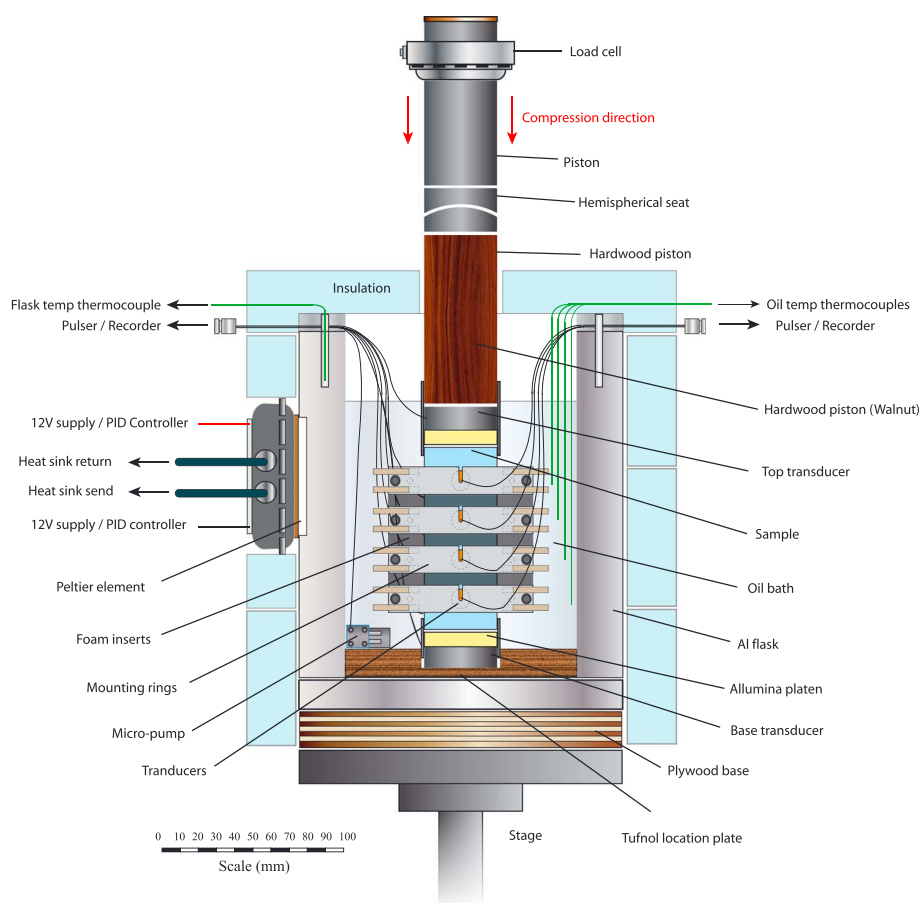
Figure 1. Schematic diagram of sample chamber and sample assembly configuration for unconfined uniaxial shortening with in situ ultrasonic measurements. The sample was immersed in a silicon oil bath. The oil temperature was controlled using a Peltier element linked to a temperature controller and *k* type thermocouple. Heat was removed by a liquid cooled heat sink designed for cooling computer components. Uniaxial compression was supplied by an Instron servohydraulic press controlled by a LabView interface. Displacement rate was controlled by a displacement transducer coupled to the piston. The transducers were coupled to the sample using spring-loaded mounting rings which provided precise positioning control and coupling. Load was recorded using an in-line load cell. Temperature was monitored and recorded on LabView using a National Instruments thermocouple module on four channels.

made rough cuts to approximate length using a band saw, and machined the samples on a lathe to produce the final cylindrical shape. The starting material had a homogeneous microstructure, a random CPO, a mean grain size of 360 µm and up to ≈1% porosity.

The sample assembly consisted of two 42 mm diameter alumina platens on either end of the sample, topped with a hardwood piston, and bounded on the bottom by a hardwood disc (Figure 1). We place a hemispherical seat between the upper wooden piston and the loading piston. These components were held in line by a custom neoprene jacket. We placed the sample assembly in an insulated, thermoelectrically cooled (Peltier ceramic) aluminum sample chamber (see *Vaughan et al.* [2016] for a full description of the sample chamber) filled with silicone oil (dimethylsiloxane, 0.965 g/cm^3), kept in circulation using a small self-priming pump (TM200S-SUB from TCS Micropumps) in order to homogenize the temperature of the cooling medium. A temperature controller (Carel IR33 Universale Proportional integral derivative (PID)) maintained the system oil temperature within ±0.5°C of the target temperature using feedback from a *k*-type thermocouple placed inside the chamber. Fluctuations in oil temperature (Figure 4c) were an order of magnitude more than those in the ice sample (supporting information Figure S2).

A uniaxial servohydraulic press was used as a deformation apparatus (Servotechnique, UCL Rock Physics Lab) with displacement rate controlled by a high-precision linear variable differential transducer (LVDT). We recorded load and displacement continuously on a LabView and national instruments data acquisition card
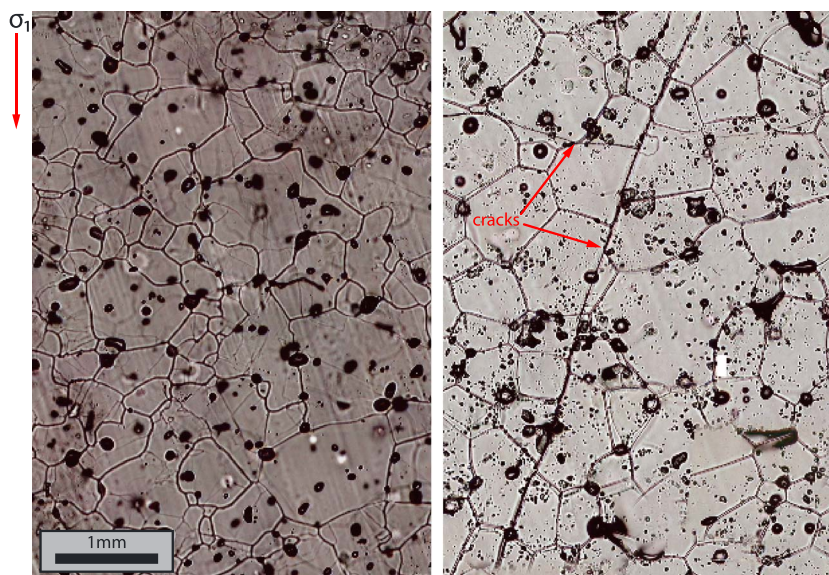
Figure 2. Optical thin section photographs from two samples following deformation. (left) An ice polycrystal deformed to 10% strain at a strain rate of $\approx 1 \times 10^{-6}$ at $-5°C$. (right) An ice polycrystal deformed to 10% strain at a strain rate $\approx 1 \times 10^{-4}$ at $-5°C$. The orientation of the shortening direction is vertical. Obvious cracks are only visible in the sample deformed at the much faster strain rate. The black speckle effect is a result of frozen droplets of water sitting between the ice thin section and the glass slide and is not in the ice volume. These ice droplets are required for mounting a thick section for preparation and are not visible in the polished surfaces of thick sections.

and converted load to stress using a linear interpolation of sample surface area from measurements of initial and final diameter (measured at top, bottom, and middle of the sample, with no observed variation >0.1 mm).

We compressed the samples uniaxially at $-5°C$ at a constant displacement rate that corresponds to an initial axial strain rate of 1×10^{-6} s^{-1} and increases (approximately linearly) to a rate of 1.1×10^{-6} s^{-1} at 10% axial engineering strain. We present results of five successful experiments that achieved final axial shortening of 1, 3, 5, 7.5, and 10% (supporting information Table S1). We chose these magnitudes in order that the microstructures of the samples at each strain step could be measured. We observed maximum stresses of ≈ 1.1 MPa, and no cracks were visible in the polished surfaces of thick sections or in optical thick sections in deformed or undeformed samples (Figure 2a). Samples deformed at higher strain rates (up to 1×10^{-4} s^{-1}) in other experiments [*Jefferd*, 2015] show clear evidence of brittle damage in optical thin sections (Figure 2b). In natural settings, strain rates are very slow ($<10^{-9}$ s^{-1}). To explore the stages of ice creep in laboratory tests, simulating the slowest deformation rates at polar conditions is impractical, since this would require very long experiments. Therefore, the creep behavior of natural ice is extrapolated from mechanical tests performed at higher temperatures or stresses [*Glen*, 1955; *Jacka and Maccagnan*, 1984; *Goldsby and Kohlstedt*, 2001; *Sammonds et al.*, 1989] and then compared with field observations.

2.2. Ultrasonic Travel Time Measurements

Using sprung mounting rings (Figure 3), we positioned and freeze-coupled eight P wave sensitive piezoelectric transducers (PZT) in aluminum casings to the sample surface. We placed two additional PZTs at the top and bottom of the sample. We performed active V_p (henceforth expressed in km/s) surveys by repeatedly generating elastic waves at a PZT using a high-frequency (1 MHz), high-voltage (250 V) pulse, while recording the transmitted waves arriving at all other PZTs positioned around the sample. Waves were pulsed on each channel in turn, while all other channels recorded (at a high sampling rate of 50 MHz, with each waveform compiled from a stack of 32 consecutive wavelets, which improves the signal-to-noise ratio). We determined arrival times from first break picks on the wavelets arriving at each PZT and converted to velocity using the ray-path lengths. In order to obtain accurate changes in travel times, we applied the waveform cross-correlation technique described in *Brantut et al.* [2011]. We used measured axial displacement and interpolation of initial and final sample diameters, measured at all sensor locations on the sample (Figure 4b), to calculate raypath
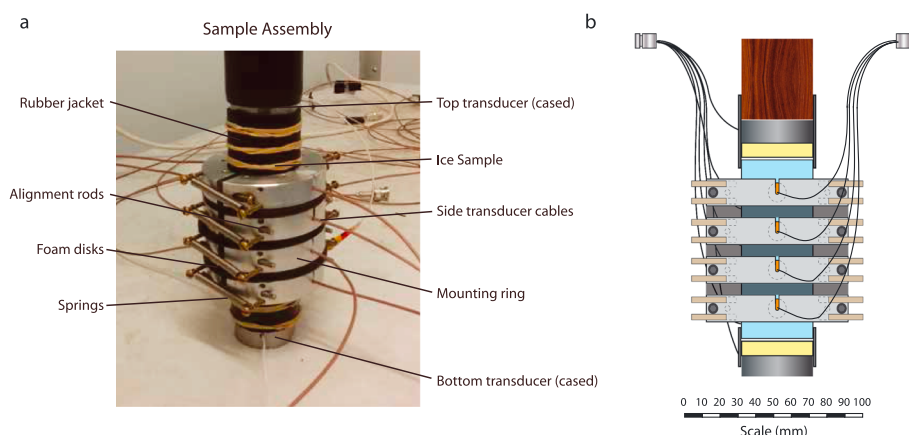
Figure 3. A photograph of the (a) sample assembly prior to deformation, (b) shown diagrammatically. The ice sample was surrounded by eight side transducers and two end transducers. Each sensor was housed in a custom aluminum casing that maintained the connection to a coaxial cable. Coupling between the sample and each sensor was maintained by spring-loaded sensor rings. The sample and pistons were held in alignment by rubber jacketing.

lengths as a function of sample shortening. Elastic length changes were too small to affect calculated velocities significantly. Adjustments for travel time through the PZT sensor casings were applied to the arrival times. We estimate the error on changes in velocity along a single raypath at $< \pm 0.01$ km/s, which relates to how accurately we could measure sample diameter. Absolute measurements of velocity can be affected
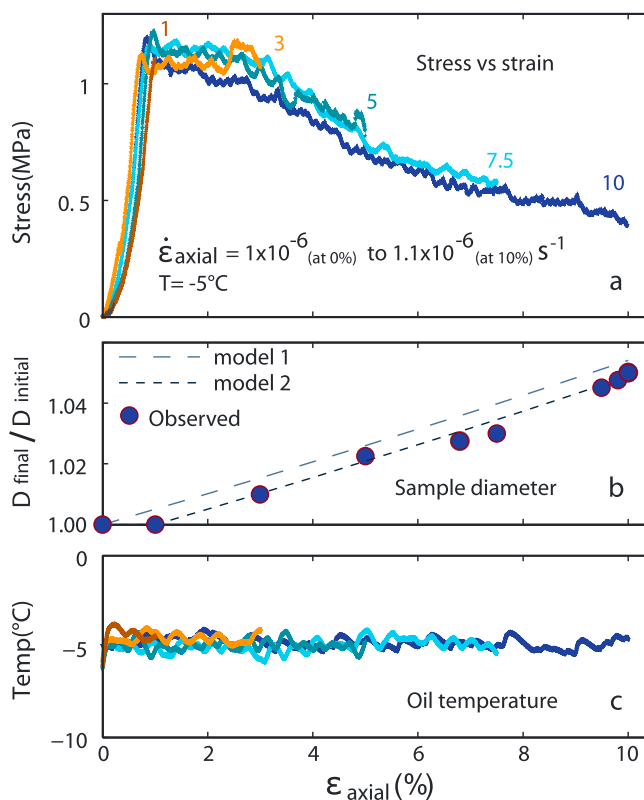
Figure 4. Stress, sample diameter, and temperature with strain, and displacement with time, during five uniaxial shortening experiments. (a) Stress versus strain curves, derived from combined load (load cell) and LVDT data. Maximum % strain for each experiment is indicated. (b) Measured sample diameters (from caliper measurements, averaged from several points on the sample) after unloading and model diameters (Model 1 = constant volume. Model 2 = no diameter change until 1% shortening, then constant volume) versus strain. (c) Oil bath temperatures were recorded throughout the experiments at four depths in the chamber, with an observed deviation of <0.1°C from the mean.

by any nonuniform distribution of porosity within the sample, or slight variations in the quality of the coupling between the sample and each transducer. We estimate these effects on absolute velocity calculations to be $< \pm 0.05$ km/s.

2.3. Cryo-EBSD

We acquired EBSD maps using a Zeiss Sigma VP FEGSEM fitted with on Oxford Instruments Nordlys camera and AZTEC software. Modifications required for cryo-EBSD are described in *Prior et al.* [2015]. We cut ≈1 cm thick, parallel-sided slices, along the cylinder axis of each deformed sample and one undeformed reference sample, and manually polished them at −60°C on fine-grit diamond disks. We removed frost and surface damage by pressure sublimation cycling in the scanning electron microscope chamber [*Prior et al.*, 2015]. We collected EBSD maps at a stage temperature of ≈ −90°C with 30 kV accelerating voltage, 60 nA beam current, 10 Pa partial pressure nitrogen at a 40 μm step size. We generated montage maps to capture large areas of the samples, with the largest maps generated being over 30 mm in their longest dimension, characterizing the majority of the sample surface and providing robust statistical parameters. The stability of the sample surface at these very low temperatures made it possible to acquire such large data sets. We processed the raw EBSD data using the band contrast as a template [*Pearce*, 2015] and generated microstructural information using the open-source MTEX toolbox [*Bachmann et al.*, 2011]. We use eigenvectors calculated from the EBSD data to describe the shape and strength of alignment of *c* axes [*Woodcock*, 1977]. The eigenvalues (magnitudes of the eigenvectors) sum to 1 and by convention a1 ≤ a2 ≤ a3.

3. Results

3.1. Mechanical Data

The stress-strain curves (Figure 4a) indicate hardening during shortening from 0 to ≈1%. At ≈1% shortening, peak stresses between 1.1 and 1.2 MPa are reached. Stresses remain at peak values up to the onset of weakening between 2.5 and 3% shortening. The maximum rate of weakening is between 3% and 5% shortening, corresponding to a stress drop to 0.75 MPa. Weakening rate decreases continually with further shortening with stresses at 0.55 to 0.6 MPa at 7.5% and 0.5 MPa at 10%. These mechanical results are comparable to those obtained in slightly faster, constant displacement rate experiments (with initial strain rates of $2-2.5 \times 10^{-6}$ s^{-1}) by *Qi et al.* [2017], on H_2O ice at −10°C, and by *Piazolo et al.* [2013] on D_2O ice at −7°C (which corresponds to −10.7°C for H_2O). In those experiments peak stresses, while higher, occurred at the same magnitudes of strain, as did the onset of weakening and the approach to quasi steady state creep (≈10% strain). In our slower, higher-temperature experiments, the samples underwent a larger degree of weakening, reducing in macroscopic strength by ≈0.5 times peak stress.

Sample diameter remains unchanged after 1% shortening and unloading. A permanent sample diameter increase is measured in all samples with 3% or more shortening (Figure 4b). These data fit a model where volume is conserved beyond 1% of uniaxial shortening (Model 2 in Figure 4b) except for results at 6.8, and 7.5% shortening where the diameter increase is less than this model predicts. The low-amplitude oscillations in stress during these experiments are related to oscillations in oil temperature of the cryostat (Figure 4c), and not to oscillation in displacement rate with time. The pattern of mechanical behavior described above is observed in repeat experiments, where samples were deformed to 10% strain under the same conditions (supporting information Figure S3).

3.2. Microstructure, Crystallographic Preferred Orientation, and Anisotropy

The content of this paper is of interest to at least three distinct research communities; glaciology, geology, and materials science. There are differences in terminology between these communities and to maximize clarity we outline briefly here our chosen terminology. CPO (crystallographic preferred orientation) is a term used extensively in the geoscience literature and is synonymous with LPO (lattice preferred orientation, also a geoscience term), COF (crystal orientation fabric, used in glaciology), fabric (used in glaciology and geology) and texture (used in material science and metallurgy). We avoid the terms fabric and texture as they have opposite meanings for geoscientists and material scientists. CPOs in ice are usually described based on the pattern of *c* axes on a stereonet (pole figure). Common patterns [e.g., *Alley*, 1992] include the following:

1. The *c* axes are subparallel to each other. We call this a cluster CPO as the points on the stereonet form a cluster or single maximum. Some glaciological literature calls this a cone, as the bounding surface of the distribution is conical.
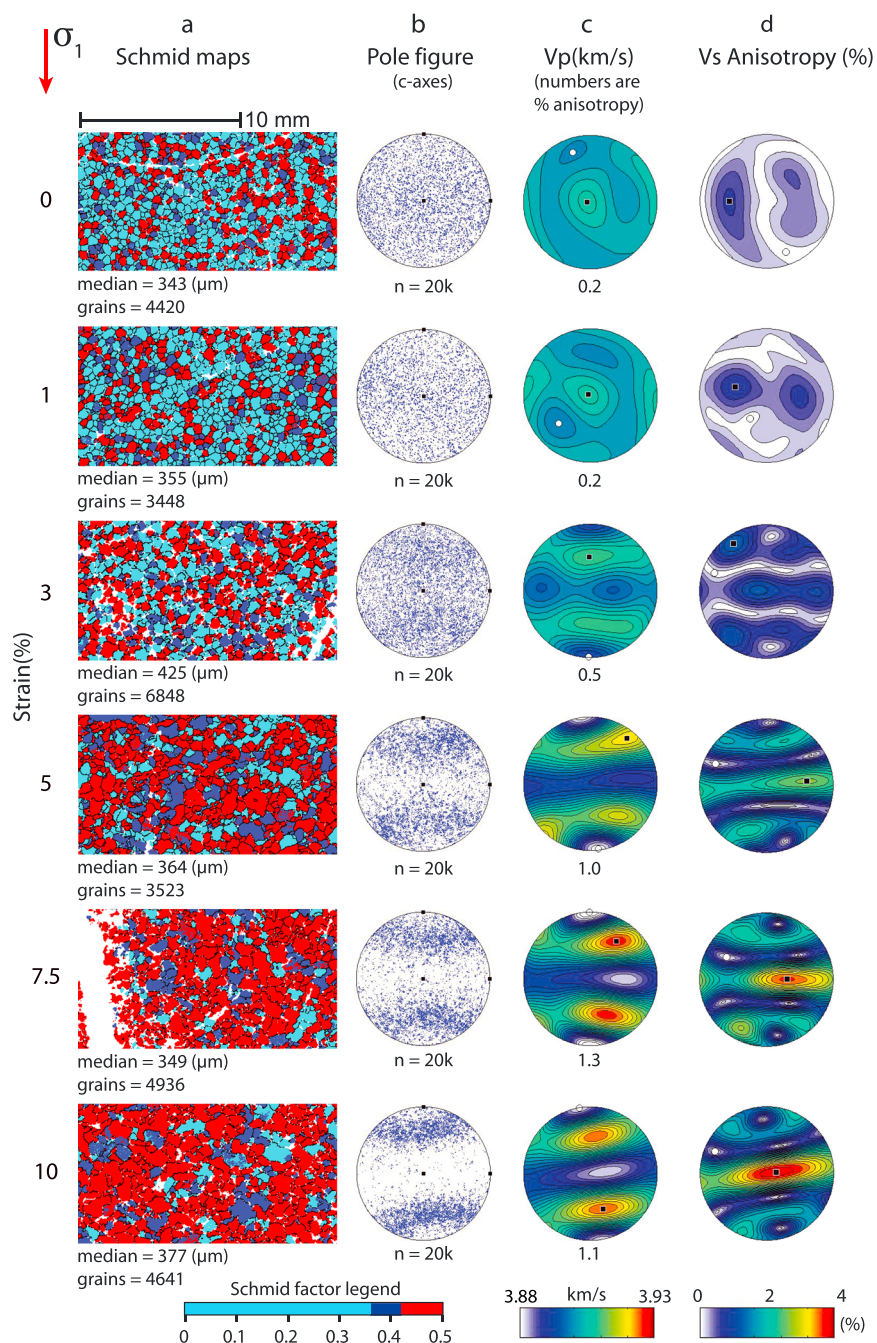
Figure 5. EBSD data sets from each deformed sample and one reference sample, with their respective pole figures and predictions of elastic wave velocity and anisotropy for each strain step, deformed at −5°C. (a) EBSD data from each sample are coloured by Schmid factor, a measure of the shear stress resolved on the basal planes (0–0.5). We show subsets of larger full data sets so that microstructural detail can be seen. Grain size data for each sample are presented as the median area equivalent diameter in micrometers, with the number of grains in each complete data set. (b) *c* axis pole figures in upper hemisphere projection, each with 2×10^4 randomly selected points from the complete data sets. (c) V_p velocity predictions from CPO, with the magnitude (%) of V_p anisotropy below each pole figure. (d) Shear wave splitting anisotropy (%) as a function of propagation direction through the sample, predicted from CPO data. The orientation of the maximum principal stress, σ_1, is vertical.
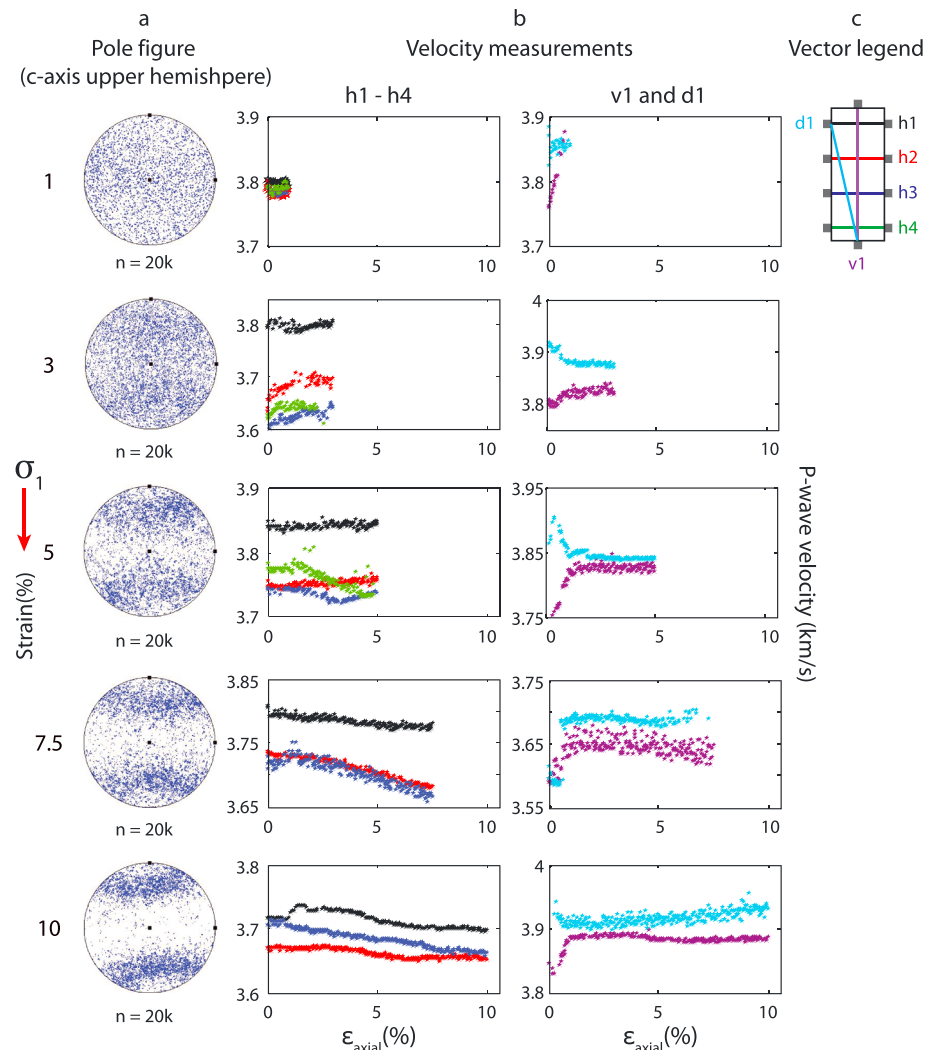
Figure 6. Evolution of V_p for multiple sample vectors for all increments of strain. (a) c axis pole figures in upper hemisphere projection for each sample. (b) In situ measurements of V_p as a function of increasing strain for each of six sample vectors, indicated by the diagram (c).

2. The c axes are distributed on a conical surface. We call this a cone CPO. The pattern of the points on a stereonet is a small circle. In the glaciological literature this pattern is often called a girdle. We avoid the term girdle as in geology it is synonymous with a planar alignment, expressed as points distributed on a great circle on a stereonet.

3. The c axes are distributed on a planar surface. We call this a planar CPO. The pattern of the points on a stereonet is a great circle.

EBSD maps colored by Schmid factor, a geometrical measurement (that assumes a uniform stress field) of the resolved shear stress (min. 0 and max. 0.5) [*Barrie et al.*, 2008; *Schmid and Boas*, 1950] on the basal plane (the easy slip system in ice) under uniaxial shortening, at each measurement point, are shown in Figure 5a. The c axis in each grain is the pole to the basal plane. The respective c axis pole figures for each sample are shown in Figure 5b. Between 0% and 1% shortening, little change is visible with no CPO development and preservation of the polygonal grain structure. By 3% shortening, a weak cone CPO is visible. Some grains have lobate or serrated boundaries and an increase in the median grain size is observed. At 5%, 7.5%, and 10% shortening, a cone CPO is well developed. Grains become increasingly interlocked, with lobate grain boundaries and irregular grain shapes dominating the microstructure by 10% strain. The strength of the CPO increases from 3% to 10% shortening.
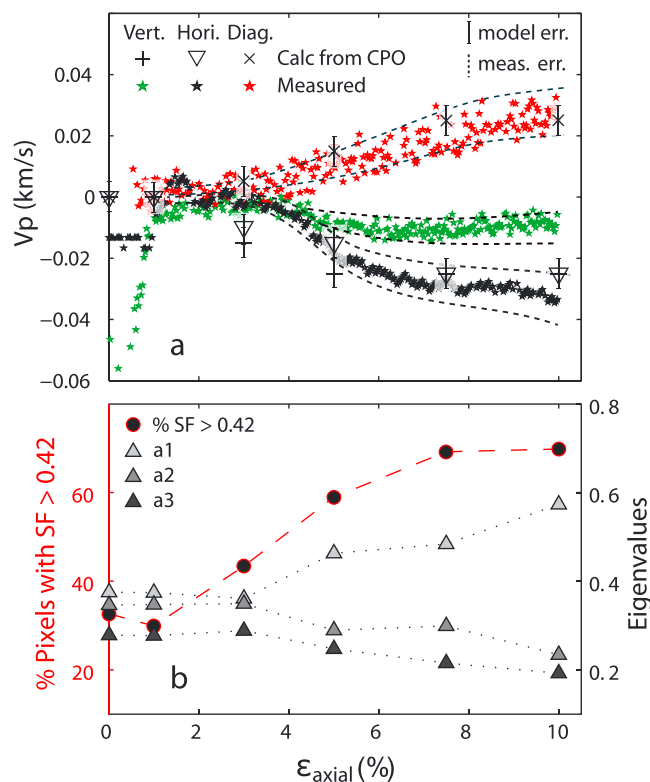
Figure 7. Evolution of V_p anisotropy in the 10% shortening experiment compares with CPO strength (eigenvalues) and Schmid factor proportion for all experiments. (a) Measured (in situ velocity surveys) and model predictions (from Cryo-EBSD) of vertical, horizontal, and diagonal vector velocity changes as a function of strain. (b) Eigenvalues (a1, a2, and a3), and % of pixels with a Schmid Factor greater than 0.42 (out of max 0.5) versus strain.

The final CPO evolves rapidly with strain from random to a cone CPO where the majority of the c axes have orientations at ≈35° to the compression direction. While the cone CPO is well developed by 10%, some grains still fall outside the cone. This observed final CPO is similar to those obtained by *Jacka and Maccagnan* [1984], *Jacka and Jun* [2000], *Piazolo et al.* [2013], *Treverrow et al.* [2012], and *Montagnat et al.* [2015] for unconfined uniaxial compression experiments. The percentage of high Schmid factor orientations increases after 1% shortening. At 3% shortening, grains with Schmid factors greater than 0.36 form an interconnected network.

We used a Voigt-Reuss-Hill (VRH) average to make theoretical predictions (in all directions through the samples) of *P* wave velocity (V_p) (Figure 5c), and shear wave splitting anisotropy (%) (Figure 5d) for the deformed samples at each deformation step. In the case of shear waves, an initially polarized shear wave will split into two orthogonally polarized, fast and slow shear waves if traveling though an anisotropic medium. The shear wave anisotropy is the difference in velocity between the two waves (here expressed in %) [*Harland et al.*, 2013]. We used the Matlab-based MTEX software package to calculate the VRH averages by combining the mildly anisotropic single-crystal elastic stiffness tensor for ice, and an orientation distribution function (ODF) of the crystals in the aggregate [*Mainprice et al.*, 2011]. An ODF is a quantitative description of sample CPO determined from EBSD orientation data and is a measure of the volume fraction of grains with a certain orientation. *Mainprice et al.* [2011] include a comprehensive review of the methods for calculating anisotropic physical properties from EBSD data using MTEX.

For the undeformed and 1% shortening samples, we predict low V_p anisotropy values of 0.2% and V_s splitting anisotropy values of 0.7–0.8%. For V_p, this value increases to 0.5% at 3% shortening, and then to values >1% at greater shortening. V_s splitting anisotropy increases to 1.3% by 3% strain and to 3.9% at 10% strain. We predict maximum value of V_p at an angle to the compression direction, where c axes orientations are localized on the cone, while we predict shear waves to be become the most anisotropic in the sample horizontal direction. The V_p predictions do not consider the temperature sensitivity of elastic waves in ice, which decrease in velocity with increasing temperature [*Kohnen and Gow*, 1979; *Vogt et al.*, 2008; *Vaughan et al.*, 2016]. We predict that

P waves propagating horizontally or vertically through the sample will show a progressive decrease in wave speeds with increasing CPO strength, while diagonal vectors are predicted to increase in velocity, approaching a maximum around 10% shortening. In the case of single cluster fabrics, one would anticipate the highest V_p raypaths to align with orientation of the cluster, as is predicted in models [*Maurel et al.*, 2015; *Diez and Eisen*, 2015] and measured in natural ice core samples [*Kohnen and Gow*, 1979; *Kohnen and Bentley*, 1977]. Indeed, *Smith et al.* [2017] were able to make interpretations of subsurface ice fabrics using field seismic observations of shear wave data (although the anisotropy of a cone CPO geometry was not considered in their analysis).

3.3. Ultrasonic Velocity Measurements

Results of the in situ velocity surveys from each experiment are presented in Figure 6 as a function of increasing strain and the evolution of CPO. Changes in V_p along a horizontal, vertical (parallel to shortening), and a diagonal wave paths through the sample are shown. V_p for the vertical and horizontal vectors shows a small increase between 0% and 1% shortening. The horizontal vectors V_p begin to decrease after 2% to 3% shortening, with most of the change developing between 3% and 7.5%. Vertical V_p remains constant from 1% to 3% shortening and then decreases with further shortening. First arrival picks on the diagonal vector in the first 1% shortening have very high uncertainties (likely due to poor coupling of the top and bottom transducers at low stress), leading to variable velocity trends. After 3% shortening the diagonal vector V_p increases with further strain.

Figure 7a compares the results of V_p anisotropy modeled from the EBSD orientations to in situ measurements of V_p, from the 10% shortening experiment. We show good agreement between calculated and measured velocity changes for the horizontal and diagonal vectors. The decrease in measured vertical velocities is less (≈0.01 km/s) than that predicted from the CPO (0.025 km/s) but shows the same trend. Most of the change in velocity develops between 3 and 7.5% shortening, corresponding to the biggest change in CPO strength as shown by *c* axis eigenvalue data [in Figure 7b *Woodcock*, 1977].

4. Discussion

The constant sample diameter, rapid increase in vertical velocities, and lack of microstructural and CPO development in the first 1% of shortening suggests that this phase is partially accommodated by pore collapse and a small component of recoverable elastic strain. This hardening stage is often referred to as "primary creep" and involves the redistribution of internal stresses between grains [*Duval et al.*, 1983] and dislocation accumulation at grain boundaries [*Montagnat et al.*, 2009]. Primary creep may also involve load transfer from easy slip to hard slip systems [*Faria et al.*, 2014] and evidence for this is rare [*Piazolo et al.*, 2015; *Vaughan*, 2017]. It is anticipated that during this stage, strain incompatibilities between the grains will lead to the accumulation of heterogeneous internal stresses [*Piazolo et al.*, 2015], and therefore heterogeneous strain, as a triggering mechanism for recrystallization.

Microstructure and CPO development starts after 1% shortening. Divergence of velocities along different elastic wave propagation directions and divergence of CPO eigenvalues does not start until 3% shortening (Figure 7b), suggesting that CPO only starts to develop and impact anisotropy at ≈3% strain. Microstructure does change between 1% and 3%, with development of lobate grain boundaries, an increase in grain size from 355 to 425 μm (median area equivalent diameter, Figure 5a), and an increase in the percentage of pixels with high Schmid factors (Figure 7b). CPO evolution likely initiates with rotation of grains toward the shortening direction by intracrystalline dislocation slip on basal planes [*Weertman*, 1973], a mechanism which alone would result in the formation of a single cluster CPO aligned with the shortening direction.

Microstructural observations in ice [*Jacka and Maccagnan*, 1984; *Duval and Castelnau*, 1995; *De La Chapelle et al.*, 1998] and other minerals [*Urai et al.*, 1986] have been used to infer that strain-induced grain boundary migration (GBM) favors the growth of grains well oriented for slip. Similarly, we infer that grains with easy slip orientations (those with high basal plane Schmid factors) grow by GBM, into neighboring grains with higher stored strain energies. Grains may rotate to high Schmid factor orientations where they are then able to grow by GBM. Grains which are in hard basal slip orientations will experience higher stress and attempt to activate nonbasal slip systems [*Chauve et al.*, 2017b], storing greater magnitudes of internal strain. This is supported by the observed progressive loss of grains in hard slip orientations with increasing strain. The consumption of grains nonsuitably oriented for easy slip by grains which are oriented in an easy slip orientation has been previously observed in experimentally deformed quartzite [*Kilian et al.*, 2011]. We infer that deformation after

≈10% is likely to proceed with the rate of grain rotation (driven by intracrystalline slip by glide on the basal planes) balanced by the rate at which easy slip grains consume other (rotated) grains. The observation that cone CPOs often evolve into a stable configuration where c axes dominantly have orientations at 35° to the shortening direction, rather than the easiest basal slip orientation of 45°, may be a product of this balance.

The final CPO configuration observed in these experiments is consistent with previous laboratory observations under similar conditions in dynamically recrystallized ice [among others, *Montagnat et al.*, 2015; *Jacka*, 1984; *Piazolo et al.*, 2013; *Jacka and Maccagnan*, 1984] where grain boundary migration recrystallization coupled with nucleation, and rotation by basal slip are considered the dominant mechanisms controlling CPO evolution.

Substantial weakening (Figure 4a) corresponds to the start of CPO formation and velocity anisotropy development at 3% shortening (Figures 5 and 7). At 3% shortening, grains with high basal Schmid factors begin to grow at the expense of grains with low basal Schmid factors and dominate the microstructure by 7.5% strain (Figure 5a). If these easy slip grains grow enough to become neighbours, forming an interconnected network of grains whose basal planes are in alignment, weakening may be accommodated by deformation along such a network of shear planes.

At least two of our experiments had a component of localized simple shear, expressed as a slight deviation along the vertical axis of the sample observed post-deformation (supporting information Table S1), and the deviation of some diameter measurements (Figure 4b) from that predicted (model 2) can be explained by components of simple shear. These minor deviations from homogeneous deformation may result from partial localization of strain on shear bands, although these are not obvious in the microstructure.

A decrease in grains size between 3 and 7.5% shortening (425 µm to 349 µm, Figure 5a) is interpreted as the contribution of nucleation mechanisms to generating new grains. Grain size increases between 7.5% and 10% shortening and is interpreted as the continued consumption, by GBM, of low Schmid factor grains that lie between networks of easy slip grains. Since grain shapes change dramatically between the undeformed (equiaxed grains of uniform size distribution) and deformed samples (highly interlocked, lobate grain shapes), a 2-D sectioning effect could account for a component of this observed change in grain size. Weakening rate reduces after 5% shortening. CPO strength (as indicted by eigenvalues) and the proportion of high Schmid factor grains approach maximum values at 10% shortening (Figure 7).

We observe that V_p anisotropy increases with increasing strain and CPO strength (as indicated by eigenvalues) and that our model predictions of V_p from EBSD are in close agreement with our in situ measurements for the horizontal and diagonal vector. V_p progressively increases on the diagonal vector as c axes of the grains become more tightly localized at an approximate 35° angle to the compression direction. This observation is similar to opening angle effects predicted by modelling [*Maurel et al.*, 2015], and physical measurements [*Gusmeroli et al.*, 2012] from vertical single maxima CPOs were velocity anisotropy increases as the single cluster CPO tightens (opening angle decreases). We find that our high-temperature cone CPO has lower predicted and measured magnitudes of V_p and V_s anisotropy than those observed or predicted for single maxima CPOs [*Maurel et al.*, 2015; *Harland et al.*, 2013]. Although our high-temperature CPOs are much less commonly observed in natural ice than are single maxima CPOs [*De La Chapelle et al.*, 1998; *Obbard et al.*, 2011], their impact on ice flow behavior could be significant. While single cluster CPOs are mechanically hard in vertical shortening, the evolution of a cone CPO leads to weakening under vertical shortening and may play an important role (particularly in high-temperature settings) if uniaxial compression dominates. It is important to recognize the change in the orientation and magnitude of seismic anisotropy that will result from a transition between single cluster and cone CPOs, as the deformation kinematics in an ice sheet vary spatially.

5. Conclusions

Changes in ultrasonic velocity during laboratory ice deformation can be used as a continuous proxy for CPO evolution and can quantify the relationship between velocity anisotropy and CPO development. Our time-lapse measurements of ultrasonic velocity in multiple directions for an evolving cone CPO match closely our predictions of anisotropy derived from EBSD data sets and reveal a detailed nonlinear increase in CPO strength and anisotropy with increasing strain. It is essential for interpretation of englacial reflections that the geometry and magnitude of anisotropy be used to discriminate between cone and cluster CPOs [*Horgan et al.*, 2011, 2008]. These two CPO geometries form under different temperature regimes and have contrasting

impacts on mechanical anisotropy, with cones leading to weakening in uniaxial shortening. While ultrasonic measurements have been used as a proxy for single clusters [*Gusmeroli et al.*, 2012], there are no such measurements for cone CPOs, nor ultrasonic measurements that reveal the complex way in which CPO and the resulting anisotropy evolve with strain under known deformation conditions.

Substantial weakening at ≈3% axial shortening at −5° C may result, in part, from the formation of a connected network of grains well oriented for basal slip. CPO development starts at the onset of weakening (3% shortening) and is close to fully developed at 10% shortening. The observed cone CPO is formed by the selective growth of easy slip grains by dislocation density-driven grain boundary migration at the expense of hard slip grains, because hard slip grains accumulate greater internal strain energy (nonbasal dislocations). Our ultrasonic observations support our suggestion that CPO does not begin to manifest until close to 3% strain. This suggests that grains in easy slip orientations may undergo rotation more readily when neighboring grains well oriented for basal slip, than when surrounded by grains in hard slip orientations. Weakening by connecting easy slip grains during recrystallization could be mechanism relevant to rocks where grain boundary migration is the dominant recrystallization process. Such weakening could be important in localization of strain in ice sheets, and the initiation of high-temperature shear zones. Additional analysis is required in order to further substantiate this network formation hypothesis.

The approach used in these experiments for real-time ultrasonic measurements during unconfined ductile creep in ice could be applied in a wider range of temperature and stress configurations. For these experiments, we chose to work at higher temperatures because the CPOs and mechanical behavior are already well known, and because the experiments can be executed relatively quickly. We do not infer a relationship to colder conditions, but these experiments are possible, although they present some practical challenges. A modification of this technique for measurements in simple shear would be of considerable value to the glaciological community.

References

Alley, R. B. (1992), Flow-law hypotheses for ice-sheet modeling, *J. Glaciol.*, *38*(129), 245–256.

Anandakrishnan, S., and R. B. Alley (1994), Ice stream C, Antarctica, sticky spots detected by microearthquake monitoring, *Ann. Glaciol.*, *20*(1), 183–186.

Ayling, M. R., P. G. Meredith, and S. A. Murrell (1995), Microcracking during triaxial deformation of porous rocks monitored by changes in rock physical properties: I. Elastic-wave propagation measurements on dry rocks, *Tectonophysics*, *245*(3), 205–221.

Azuma, N. (1995), A flow low for anisotropic polycrystalline ice under uniaxial compressive deformation, *Cold Reg. Sci. Technol.*, *23*(2), 137–147, doi:10.1016/0165-232x(94)00011-l.

Bachmann, F., R. Hielscher, and H. Schaeben (2011), Grain detection from 2D and 3D EBSD data—Specification of the MTEX algorithm, *Ultramicroscopy*, *111*(12), 1720–1733, doi:10.1016/j.ultramic.2011.08.002.

Bamber, J. L., D. G. Vaughan, and I. Joughin (2000), Widespread complex flow in the interior of the Antarctic Ice Sheet, *Science*, *287*(5456), 1248–1250, doi:10.1126/science.287.5456.1248.

Barrie, C., A. Boyle, S. Cox, and D. J. Prior (2008), Slip systems and critical resolved shear stress in pyrite: An electron backscatter diffraction (EBSD) investigation, *Mineral. Mag.*, *72*(6), 1181–1199.

Bentley, C. R. (1972), Seismic-wave velocities in anisotropic ice: A comparison of measured and calculated values in and around the deep drill hole at Byrd Station, Antarctica, *J. Geophys. Res.*, *77*(23), 4406–4420.

Brantut, N., A. Schubnel, and Y. Gueguen (2011), Damage and rupture dynamics at the brittle-ductile transition: The case of gypsum, *J. Geophys. Res.*, *116*, B01404, doi:10.1029/2010jb007675.

Brantut, N., M. J. Heap, P. Baud, and P. G. Meredith (2014), Mechanisms of time-dependent deformation in porous limestone, *J. Geophys. Res. Solid Earth*, *119*, 5444–5463, doi:10.1002/2014JB011186.

Budd, W., and T. Jacka (1989), A review of ice rheology for ice sheet modelling, *Cold Reg. Sci. Technol.*, *16*(2), 107–144.

Chauve, T., M. Montagnat, F. Barou, K. Hidas, A. Tommasi, and D. Mainprice (2017a), Investigation of nucleation processes during dynamic recrystallization of ice using cryo-EBSD, *Philos. Trans. R. Soc. A: Mathe., Phys. Eng. Sci.*, *375*, 20150345, doi:10.1098/rsta.2015.0345.

Chauve, T., M. Montagnat, S. Piazolo, B. Journaux, J. Wheeler, F. Barou, D. Mainprice, and A. Tommasi (2017b), Non-basal dislocations should be accounted for in simulating ice mass flow, *Earth Planet. Sci. Lett.*, *473*, 247–255.

Cyprych, D., S. Piazolo, C. J. Wilson, V. Luzin, and D. J. Prior (2016), Rheology, microstructure and crystallographic preferred orientation of matrix containing a dispersed second phase: Insight from experimentally deformed ice, *Earth Planet. Sci. Lett.*, *449*, 272–281.

De La Chapelle, S., O. Castelnau, V. Lipenkov, and P. Duval (1998), Dynamic recrystallization and texture development in ice as revealed by the study of deep ice cores in Antarctica and Greenland, *J. Geophys. Res.*, *103*, 5091–5105.

Diez, A., and O. Eisen (2015), Seismic wave propagation in anisotropic ice. Part 1: Elasticity tensor and derived quantities from ice-core properties, *The Cryosphere*, *9*(1), 367–384.

Duval, P., and O. Castelnau (1995), Dynamic recrystallization of ice in polar ice sheets, *J. Phys. IV*, *5*(C3), C3-197 – C3-205.

Duval, P., M. F. Ashby, and I. Anderman (1983), Rate-controlling processes in the creep of polycrystalline ice, *J. Phys. Chem.*, *87*(21), 4066–4074.

Duval, P., M. Montagnat, F. Grennerat, J. Weiss, J. Meyssonnier, and A. Philip (2010), Creep and plasticity of glacier ice: A material science perspective, *J. Glaciol.*, *56*(200), 1059–1068.

Faria, S. H., I. Weikusat, and N. Azuma (2014), The microstructure of polar ice. Part II: State of the art, *J. Struct. Geol.*, *61*, 21–49, doi:10.1016/j.jsg.2013.11.003.

Fortin, J., Y. Guéguen, and A. Schubnel (2007), Effects of pore collapse and grain crushing on ultrasonic velocities and VP/VS, *J. Geophys. Res.*, *112*, B08207, doi:10.1029/2005JB004005.

Fortin, J., S. Stanchits, S. Vinciguerra, and Y. Guéguen (2011), Influence of thermal and mechanical cracks on permeability and elastic wave velocities in a basalt from Mt. Etna volcano subjected to elevated pressure, *Tectonophysics*, *503*(1), 60–74, doi:10.1016/j.tecto.2010.09.028.

Glen, J. W. (1955), The creep of polycrystalline ice, *Philos. Trans. R. Soc. London, Ser. A*, *228*(1175), 519–538.

Goldsby, D., and D. Kohlstedt (2001), Superplastic deformation of ice: Experimental observations, *J. Geophys. Res.*, *106*(B6), 11,017–11,030.

Guillaume, S., J. D. Mouza, and J. Brulhet (1997), The use of ultrasonics to monitor long-term creep tests of salt rock samples, *Geol. Soc., London, Eng. Geol. Spec. Publ.*, *12*(1), 373–380.

Gusmeroli, A., E. C. Pettit, J. H. Kennedy, and C. Ritz (2012), The crystal fabric of ice from full-waveform borehole sonic logging, *J. Geophys. Res.*, *117*, F03021, doi:10.1029/2012JF002343.

Harland, S. R., J. M. Kendall, G. W. Stuart, G. E. Lloyd, A. F. Baird, A. M. Smith, H. D. Pritchard, and A. M. Brisbourne (2013), Deformation in Rutford ice stream, West Antarctica: Measuring shear-wave anisotropy from icequakes, *Ann. Glaciol.*, *54*(64), 105–114, doi:10.3189/2013AoG64A033.

Hirao, M., T. Morishita, and H. Fukuoka (1990), Ultrasonic velocity change with creep damage in copper, *Metall. Trans. A*, *21*(6), 1725–1732.

Horgan, H. J., S. Anandakrishnan, R. B. Alley, L. E. Peters, G. P. Tsoflias, D. E. Voigt, and J. P. Winberry (2008), Complex fabric development revealed by englacial seismic reflectivity: Jakobshavn Isbræ, Greenland, *Geophys. Res. Lett.*, *35*, L10501, doi:10.1029/2008GL033712.

Horgan, H. J., S. Anandakrishnan, R. B. Alley, P. G. Burkett, and L. E. Peters (2011), Englacial seismic reflectivity: Imaging crystal-orientation fabric in West Antarctica, *J. Glaciol.*, *57*(204), 639–650.

Hudleston, P. J. (2015), Structures and fabrics in glacial ice: A review, *J. Struct. Geol.*, *81*, 1–27.

Jacka, T. (1984), Laboratory studies on relationships between ice crystal size and flow rate, *Cold Reg. Sci. Technol.*, *10*(1), 31–42.

Jacka, T., and M. Maccagnan (1984), Ice crystallographic and strain rate changes with strain in compression and extension, *Cold Reg. Sci. Technol.*, *8*(3), 269–286.

Jacka, T. H., and L. Jun (2000), Flow rates and crystal orientation fabrics in compression of polycrystalline ice at low temperatures and stresses, in *Physics Ice Core Records*, edited by T. Hondoh, pp. 83–102, Hokkaido Univ. Press, Sopporo.

Jefferd, M. (2015), Relating the evolution of microstructures during the uniaxial deformation of standard ice to seismic anisotropy, Master's thesis, Dep. of Earth Sciences, Univ. College London, London, U. K.

Kilian, R., R. Heilbronner, and H. Stünitz (2011), Quartz microstructures and crystallographic preferred orientation: Which shear sense do they indicate?, *J. Struct. Geol.*, *33*(10), 1446–1466.

Kluskiewicz, D., E. D. Waddington, S. Anandakrishnan, D. E. Voigt, K. Matsuoka, and M. P. McCarthy (2017), Sonic methods for measuring crystal orientation fabric in ice, and results from the West Antarctic Ice Sheet (WAIS) divide, *J. Glaciol.*, 1–15, doi:10.1017/jog.2017.20.

Kohnen, H., and C. Bentley (1977), Ultrasonic measurements on ice cores from Ross Ice Shelf, Antarctica, drill hole, *Antarct. J. US*, *12*(4), 148–150.

Kohnen, H., and A. J. Gow (1979), Ultrasonic velocity investigations of crystal anisotropy in deep ice cores from Antarctica, *J. Geophys. Res.*, *84*(C8), 4865–4874.

Llorens, M.-G., A. Griera, P. D. Bons, R. A. Lebensohn, L. A. Evans, D. Jansen, and I. Weikusat (2016), Full-field predictions of ice dynamic recrystallisation under simple shear conditions, *Earth Planet. Sci. Lett.*, *450*, 233–242.

Mainprice, D., R. Hielscher, and H. Schaeben (2011), Calculating anisotropic physical properties from texture data using the MTEX open source package, *Geol. Soc. London, Spec. Publ. Geol. Soc.*, *360*, 175–192.

Maurel, A., F. Lund, and M. Montagnat (2015), Propagation of elastic waves through textured polycrystals: Application to ice, *Proc. R. Soc. London, Ser. A*, *471*, 20140988.

Montagnat, M., G. Durand, and P. Duval (2009), Recrystallization processes in granular ice, *Phys. Ice Core Records II*, *68*, 81–90.

Montagnat, M., N. Azuma, D. Dahl-Jensen, S. Fujita, S. Gillet-Chaulet, D. Samyn, A. Svensson, and I. Weikusat (2014), Fabric along the NEEM ice core, Greenland: Comparison with GRIP and NGRIP ice cores, *Cryosphere Discuss.*, *8*(1), 307–335.

Montagnat, M., T. Chauve, F. Barou, A. Tommasi, B. Beausir, and C. Fressengeas (2015), Analysis of dynamic recrystallization of ice from EBSD orientation mapping, *Front. Earth Sci.*, *3*, 81.

Obbard, R., K. Sieg, I. Baker, D. Meese, and G. Catania (2011), Microstructural evolution in the fine-grained region of the Siple Dome (Antarctica) ice core, *J. Glaciol.*, *57*(206), 1046–1056.

Pearce, M. A. (2015), EBSDinterp 1.0: A MATLAB((r)) program to perform microstructurally constrained interpolation of EBSD data, *Microsc. Microanal.*, *21*(4), 985–993, doi:10.1017/s1431927615000781.

Peternell, M., and C. J. Wilson (2016), Effect of strain rate cycling on microstructures and crystallographic preferred orientation during high-temperature creep, *Geology*, *44*(4), 279–282.

Peternell, M., M. Dierckx, C. J. Wilson, and S. Piazolo (2014), Quantification of the microstructural evolution of polycrystalline fabrics using FAME: Application to in situ deformation of ice, *J. Struct. Geol.*, *61*, 109–122.

Piazolo, S., C. J. Wilson, V. Luzin, C. Brouzet, and M. Peternell (2013), Dynamics of ice mass deformation: Linking processes to rheology, texture, and microstructure, *Geochem. Geophys. Geosyst.*, *14*(10), 4185–4194, doi:10.1002/ggge.20246.

Piazolo, S., M. Montagnat, F. Grennerat, H. Moulinec, and J. Wheeler (2015), Effect of local stress heterogeneities on dislocation fields: Examples from transient creep in polycrystalline ice, *Acta Mater.*, *90*, 303–309.

Picotti, S., A. Vuan, J. M. Carcione, H. J. Horgan, and S. Anandakrishnan (2015), Anisotropy and crystalline fabric of Whillans Ice Stream (West Antarctica) inferred from multicomponent seismic data, *J. Geophys. Res. Solid Earth*, *120*, 4237–4262, doi:10.1002/2014JB011591.

Pollard, D., and R. M. DeConto (2009), Modelling West Antarctic Ice Sheet growth and collapse through the past five million years, *Nature*, *458*(7236), 329–U89, doi:10.1038/nature07809.

Prior, D. J., et al. (2015), Making EBSD on water ice routine, *J. Microsc.*, *259*(3), 237–256, doi:10.1111/jmi.12258.

Qi, C., D. Goldsby, and D. Prior (2017), The down-stress transition from cluster to cone fabrics in experimentally deformed ice, *Earth Planet. Sci. Lett.*, *471*, 136–147, doi:10.1016/j.epsl.2017.05.008.

Rignot, E., J. Mouginot, and B. Scheuchl (2011), Ice flow of the antarctic ice sheet, *Science*, *333*(6048), 1427–1430, doi:10.1126/science.1208336.

Sammonds, P., S. Murrell, and M. Rist (1989), Fracture of multi-year sea ice under triaxial stresses: Apparatus description and preliminary results, *J. Offshore Mech. Arct. Eng.*, *111*(3), 258–263.

Schmid, E., and W. Boas (1950), *Plasticity of Crystals*, p. 353, F. A. Hughes and Co. Ltd., London.

Schulson, E. M., et al. (2009), *Creep and Fracture of Ice*, vol. 1, Cambridge Univ. Press, Cambridge.

Smith, E. C., A. F. Baird, J. M. Kendall, C. Martín, R. S. White, A. M. Brisbourne, and A. M. Smith (2017), Ice fabric in an Antarctic ice stream interpreted from seismic anisotropy, *Geophys. Res. Lett.*, *44*, 3710–3718, doi:10.1002/2016GL072093.

Stanchits, S., et al. (2010), *Formation of Faults in Diorite and Quartzite Samples Extracted From a Deep Gold Mine (South Africa)*, vol. 12, p. 5605, EGU General Assembly Conference, Vienna.

Stern, L. A., W. B. Durham, and S. H. Kirby (1997), Grain-size-induced weakening of H_2O ices I and II and associated anisotropic recrystallization, *J. Geophys. Res.*, *102*(B3), 5313–5325.

Tang, S., S. Wu, M. Kobayashi, and H. Pan (2007), Effects of texture evolutions and point defects on ultrasonic waves under simple shear and pure shear, *Int. J. Solids Struct.*, *44*(3), 1277–1290.

Thorsteinsson, T., J. Kipfstuhl, and H. Miller (1997), Textures and fabrics in the GRIP ice core, *J. Geophys. Res.*, *102*(C12), 26,583–26,599.

Treverrow, A., W. F. Budd, T. H. Jacka, and R. C. Warner (2012), The tertiary creep of polycrystalline ice: Experimental evidence for stress-dependent levels of strain-rate enhancement, *J. Glaciol.*, *58*(208), 301–314.

Treverrow, A., R. C. Warner, W. F. Budd, T. Jacka, and J. L. Roberts (2015), Modelled stress distributions at the Dome Summit South borehole, Law Dome, East Antarctica: A comparison of anisotropic ice flow relations, *J. Glaciol.*, *61*(229), 987–1004.

Urai, J., W. Means, and G. Lister (1986), Dynamic recrystallization of minerals, in *Mineral and Rock Deformation: Laboratory Studies: The Paterson Volume*, pp. 161–199, AGU Geophys. Monogr., Washington, D. C.

Vaughan, M. J., K. van Wijk, D. J. Prior, and M. H. Bowman (2016), Monitoring the temperature-dependent elastic and anelastic properties in isotropic polycrystalline ice using resonant ultrasound spectroscopy, *Cryosphere*, *10*(6), 2821–2829, doi:10.5194/tc-10-2821-2016.

Vaughan, M. J. H. (2017), The creep behaviour, and elastic and anelastic properties of polycrystalline ice, PhD thesis, Dep. of Earth Sciences, Univ. of Otago, Dunedin, New Zealand.

Vélez, J. A., G. P. Tsoflias, R. A. Black, C. J. Van der Veen, and S. Anandakrishnan (2016), Distribution of preferred ice crystal orientation determined from seismic anisotropy: Evidence from Jakobshavn Isbræ and the North Greenland Eemian Ice Drilling facility, Greenland, *Geophysics*, *81*(1), WA111–WA118.

Vogt, C., K. Laihem, and C. Wiebusch (2008), Speed of sound in bubble-free ice, *J. Acoust. Soc. Am.*, *124*(6), 3613–3618.

Weertman, J. (1973), Creep of ice, in *Physics and Chemistry of Ice*, vol. Ottawa, pp. 320–337, R. Soc. Canada.

Wilson, C. J., V. Luzin, S. Piazolo, M. Peternell, and D. Hammes (2015), Experimental deformation of deuterated ice in 3D and 2D: Identification of grain-scale processes, *Proc. R. Soc. Victoria*, *127*(1), 99–104.

Wilson, C. J. L., M. Peternell, S. Piazolo, and V. Luzin (2014), Microstructure and fabric development in ice: Lessons learned from in situ experiments and implications for understanding rock evolution, *J. Struct. Geol.*, *61*, 50–77, doi:10.1016/j.jsg.2013.05.006.

Woodcock, N. H. (1977), Specification of fabrics shapes using an eigenvalue method, *Geol. Soc. Am. Bull.*, *88*(9), 1231–1236.

Zwinger, T., M. Schäfer, C. Martín, and J. C. Moore (2014), Influence of anisotropy on velocity and age distribution at Scharffenbergbotnen blue ice area, *Cryosphere*, *8*(2), 607–621.